Conceptual Level Optimization of a Fan Stage Under Distortion Considering Aero-structural Constraints

Manish Pokhrel*, Darshan Sarojini*, Dimitri N. Mavris†
Daniel Guggenheim School of Aerospace Engineering,
Georgia Institute of Technology, Atlanta, Georgia, 30332

Rotor blades experience unsteady forces and aerodynamic losses when operating in a distorted inflow. The structural analysis of rotors under these conditions, therefore, is of prime importance during the early design phase. In a companion paper, an extension to the multi-meanline method for conceptual fan stage design in a non-axisymmetric flow field has been presented. Here, the authors present a computationally efficient design framework that links the aerodynamic design and structural analysis of the rotor. Rotor structural analysis comprises of computing dynamic stresses, the excitation frequencies, and resonance margins at various modes of vibration. A design space encapsulating fan stage design variables, aerodynamic performance, and rotor structural constraints is explored and optimized for maximum fan stage efficiency subject to aerodynamic and mechanical constraints.

I. Introduction

Traditional fan design processes do not account for flow asymmetry in early design phases. When operating in a distorted flowfield, as in the case of boundary layer ingestion (BLI), the flow is spatially non-uniform. In BLI propulsor modeling, many studies use representative fan maps and scale them accordingly.[1–3] Sometimes, a small drop is efficiency is assumed to model BLI losses.[4] Most BLI studies have focused on fan modeling rather than design and the unsteady response of the fan is usually ignored.[5,6] The effects of the non-uniformities and unsteady forces, therefore, cannot be ignored.

While aerodynamic performance of the fan is the objective function, the mechanical integrity is a constraint. Cousins[7] analyzed a rotor that was designed for under-wing engines and found that there were crossings of concern (or narrow resonance margins) at speeds near the design point. The greatest concerns were the excitation frequencies of lower order. Cumpsty[8] also notes that low-order excitation frequencies pose more concerns than high-order excitation frequencies. In order to avoid the crossing of natural frequency and excitation frequency, measures can be take to change these frequencies. In conventional design process, the mechanical integrity of blades is estimated using empirical relationships, and detailed structural analysis is performed in the later stages of design process. This makes sense when flow around the annulus is uniform (or can approximated to be). However, for applications like BLI, the assumption is not valid anymore. Although preferred in terms of their numerical results, 3-D FEM methods are not suitable to be used in the conceptual design due to their computational expense. In a prior work, it has been shown that Variational Asymptotic Method (VAM) can be used in the dynamic analysis of fan rotor blades.[9]

From the discussions above, it is clear that fans should be designed for asymmetry, and structural constraints need to be included during early phases of design. In this paper, a computational framework that captures the fan aerodynamic design approach[10] and rotor structural analysis using VAM[9] is introduced and explained. Section II provides a detailed discussion on the components of the framework to produce an optimal fan stage. Section III and IV discuss the test case setup and the corresponding results respectively using the framework introduced. The conclusions of the work are presented in Section V.

*PhD Candidate, Aerospace Systems Design Laboratory, AIAA Student Member
†S.P. Langley Distinguished Regents Professor, Aerospace Systems Design Laboratory, AIAA Fellow

II. Computational Framework

Figure 1 presents the notional design structure matrix for the proposed framework, generated using the XDSM tool.[11] The conceptual design of the fan stage considering aerodynamics is described in Section II A. The analysis also computes the unsteady loads that the blades would be subjected to. This process is described in Section II B. Geometrical representation of the fan is discussed in Section II C. Description of structural analysis process based on Variational Asymptotic Beam Sectional Analysis (VABS) and Geometrically Exact Beam Theory (GEBT) is presented in Section II D. The computation of structural constraints are described in Section II E. Details concerning exploration and optimization of the variables follow in Section II F.

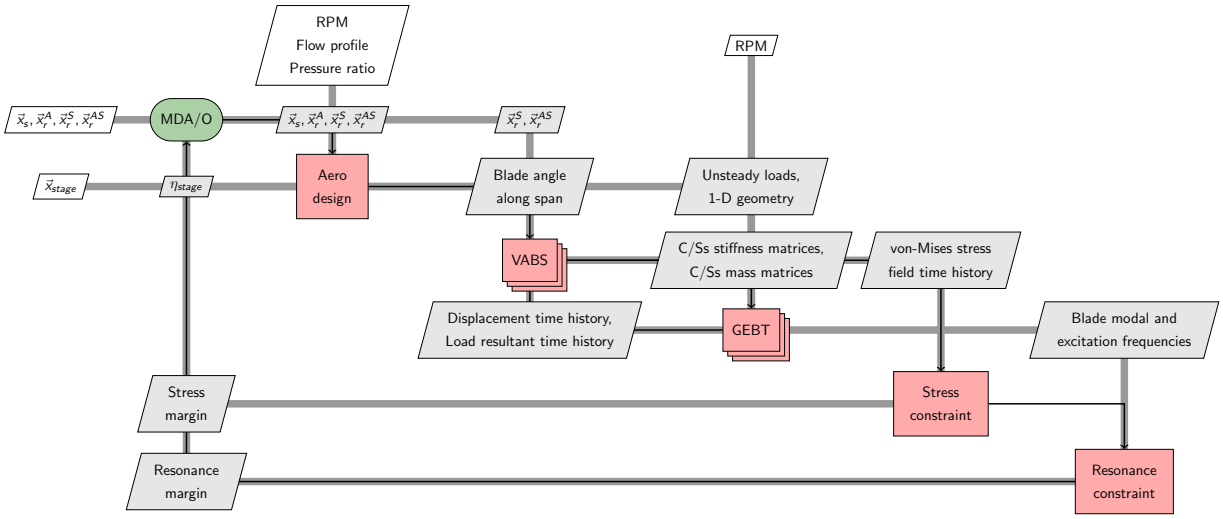

Figure 1. Extended design structure matrix of the framework.

A. Aerodynamic Design of Fan Stage

The details of the aerodynamic design process of a fan stage in the conceptual level is described in a companion paper.[10] A brief summary is presented here. As shown in Fig. 1, the flow information at the Aerodynamic Interface Plane (AIP) is assumed to be known and a stage pressure rise is a set requirement from the cycle analysis. For each set of high level fan stage design variables that the optimizer provides, the goal of this design process is to produce a blade with maximum stage efficiency. In doing so, the stagger and the blade metal angles of the rotor across the predefined number of radial segments along the span are determined. In addition, it also produces a non-axisymmetric stator whose metal angles vary circumferentially. These output variables define the rotor geometry and the corresponding loads acting on the blades. Fig. 2 shows the schematic of the approach. The design approach can be summarized in four steps:

1. Rotor design considering asymmetric flow
2. Unsteady rotor response from quasisteady response
3. Non-axisymetric stator design
4. Loop to vary the rotor design in 1 until target pressure rise is achieved

With the information of the circumferentially non-uniform flow properties at the fan face available, the first step involves designing a rotor row for the circumferentially averaged inflow for a prescribed enthalpy change. Equations of radial equilibrium, mass continuity, and Euler Turbomachinery are solved to produce the blade angles for the prescribed enthalpy change. The designed rotor is evaluated in the off-design mode and the true rotor losses are computed. Here, the off-design mode refers to the true operating condition with non-uniformities. Non-uniform flow is simulated by dividing the smooth non-uniform flow into discrete

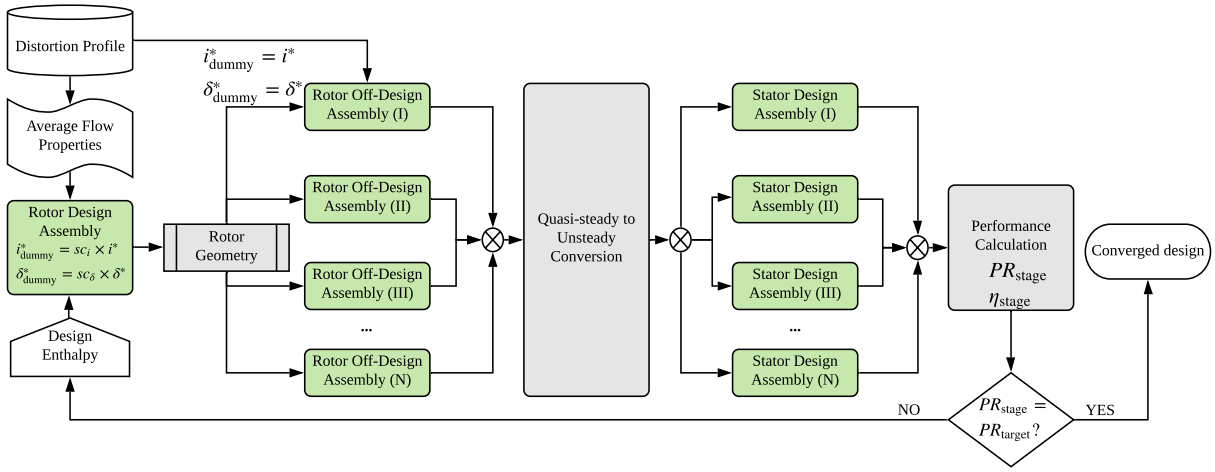

Figure 2. Fan stage aerodynamic design framework.

uniform circumferential sectors. Since the losses in the non-uniform flow are likely different from the losses in the averaged flow, the rotor design is changed until the true rotor losses are minimized. This is achieved by introducing two scalars that modify the incidence and deviation angles in the rotor design mode only. Recalling that the design mode is not the true operating point, the efficiency in the design mode intentionally designed to be non-optimal so that the blade angles are optimal when operating in the off-design mode.

The time varying incidence angle on the fan blades as they rotate in the spatially non-uniform flow results in unsteadiness. The departure of the aerodynamic performance from a quasi-steady performance depends on the per-rev distortion patterns, the extent of distortion, and finally the rate of incidence variation. The assumption that the fan blades respond to the incoming flow instantaneously is not necessarily true. The multi-meanline approach predicts the quasisteady rotor response. Assuming that the distortion is steady state and that the losses are accounted for by quasi-steady calculations, the work by Carta[12] is used to compute the unsteady rotor response. First, the quasi-steady performance of the rotor is computed. The flow properties at the rotor exit and inlet can be used to compute the axial and tangential forces. These forces can then be normalized and written in terms of coefficients of axial and tangential forces. The lift and drag coefficients can be obtained from force coefficients. The lift and drag coefficients of the rotor are compared with the lift and drag coefficients of the airfoil and a relationship is obtained. The airfoil unsteady lift and drag is computed and the same relationship is used to obtain the rotor unsteady lift and drag coefficients. The reverse calculation is performed to backtrack the unsteady force coefficients, forces, and finally the unsteady flow parameters.

For the design of non-axisymmetric stators, a multi-point multi-meanline method is used. The multi-point method treats each circumferential location separately the same way the rotor was treated, except in this case, the equations for design (and not off-design) mode are solved, the idea being that the stator has to match to the incoming flow from rotor exit.

A Newton's solver is used to vary the prescribed design enthalpy rise such that the actual stage pressure rise matches the required pressure rise. Using the flow properties from the converged calculations, loads acting on the rotor can be computed.

B. Computation of Loads

The aerodynamic module provides the flow information at the rotor inlet and exit. These flow properties are responsible for exerting forces on the rotor. As seen in Fig. 1, the unsteady loads from the aerodynamic module passes on to the structural module. The computation of aerodynamic loads from the flow parameters is described here. Consider a rotor rotating at an angular velocity, ω. The rotor is shown in Fig. 3 represented as a disk for simplicity. A fluid particle enters the rotor at a radius r_1 with absolute velocity V_1, and exits the rotor at radius r_2 with absolute velocity V_2. Here station 1 and 2 are the rotor inlet and exit respectively.

The axial force provided by the rotor is the sum of the force due to change in axial momentum and

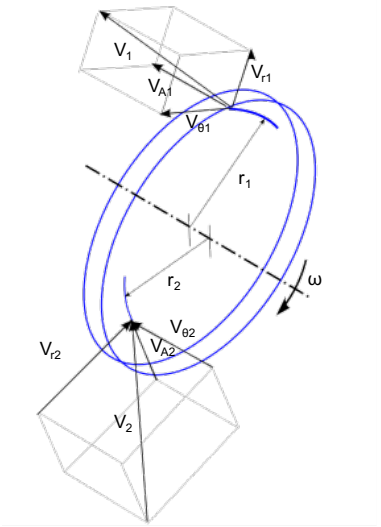

Figure 3. A rotor represented as a wheel.

change in static pressure across the rotor. Subscript A refers to the axial property. The axial force is given by Eq. 1, where F_{AH} refers to the axial force due to momentum change and F_{AP} refers to the axial force due to pressure change.

$$F_A = F_{AH} + F_{AP} \tag{1}$$

The axial force due to momentum change through a blade passage across a rotor is given by Eq. 2, where $\Delta\dot{m}$ refers to the mass flow through the blade passage and $A_{passage}$ is the blade passage area.

$$F_{AH} = \Delta\dot{m}_1 V_{A1} - \Delta\dot{m}_2 V_{A2} = A_{\text{passage}}(\rho_1 V_{A1}^2 - \rho_2 V_{A2}^2) \tag{2}$$

The axial force due to pressure difference is given by Eq. 3

$$F_{AP} = A_{\text{passage}}(p_2 - p_1) \tag{3}$$

From Eqns. 2 and 3, Eq. 1 can be written as:

$$F_A = A_{\text{passage}}(p_2 - p_1) + A_{\text{passage}}(\rho_1 V_{A1}^2 - \rho_2 V_{A2}^2) \tag{4}$$

Similarly, the tangential force can be computed by the change in the tangential momentum of the flow across the rotor, which is given by Eq. 5, where V_θ represents the swirl velocity.

$$F_\theta = \Delta\dot{m}_1 V_{\theta 1} - \Delta\dot{m}_2 V_{\theta 2} = A_{\text{passage}}(\rho_1 V_{A1} V_{\theta 1} - \rho_2 V_{A2} V_{\theta 2}) \tag{5}$$

The centripetal force (F_r) acting along the span of the rotor can also be calculated from the angular velocity of the blades. Since the inlet and exit flow properties are different at various locations, these forces are functions of the circumferential location (θ).

$$F_\theta, F_A, F_r = f(\theta, r) \tag{6}$$

Given Eq. 6 and angular frequency (ω), these forces can be converted to functions of time, as shown in Eq. 7.

$$F_\theta, F_A, F_r = f(t) \tag{7}$$

As shown in Fig. 2, the loading behavior is different for every design since the rotor exit flow parameters are defined from the work provided by the blades. The following section discusses the geometrical representation of the fan blade produced from the aerodynamic design block.

C. Geometrical Representation of the Fan Blade

The blade design is achieved by solving the equations of radial equilibrium, mass continuity, and energy at each radial blade segment. This results in the determination of blade angles at the exit and the inlet, the stagger, and the stream's radial location. Fig. 4 shows the blade angles at the inlet and the exit. A double circular arc airfoil is used to create the camber line and thickness to chord ratio defined from the aerodynamic module is used to draw the pressure and suction sides of the airfoil.

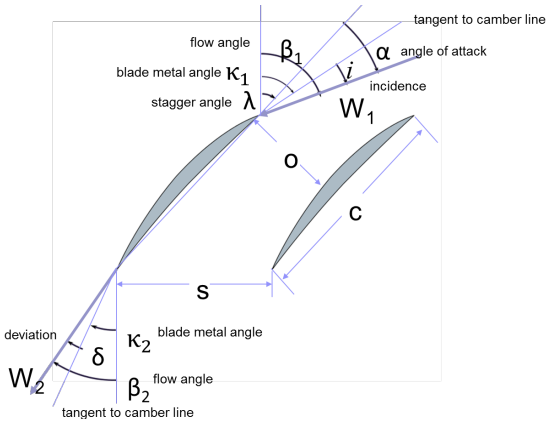

Figure 4. Cross-section definition from blade angles.

This process is repeated for each cross-section, there will be as many cross-sections as the number of radial segments used in the design process. The cross-sections can be stacked and a 3-D skeleton of the blade geometry can be formed as shown in Fig. 5.

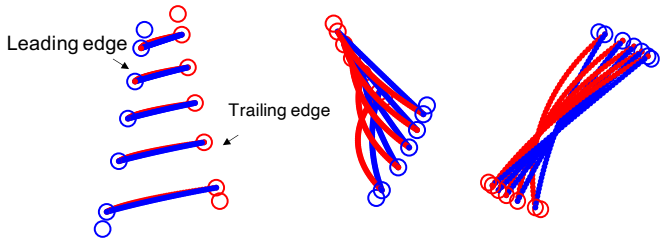

Figure 5. 3-D skeleton of the blade: hub to tip [left], obliqueness [center], twist [right].

Lofting these cross-sections, a full 3-D structure of the blade can be formed. An example is the blade shown in Fig. 6 that was lofted using the 3-D skeleton from Fig. 5.

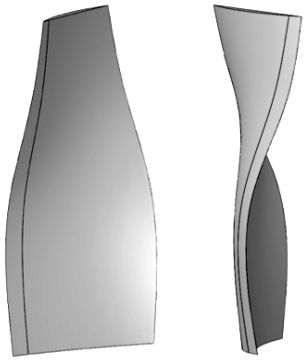

Figure 6. Lofted 3-D model of the fan blade.

D. Structural Analysis

The time varying loads calculated in Section II B act on the blade designed as described in Section II C. As a result of the unsteady loads in the design point, the steady analysis of the blade structure is not sufficient even for the conceptual phase. As shown in Fig. 1, these information is needed to perform structural analysis of the rotor blade. The use of computationally expensive finite element method (FEM) at early conceptual design is computationally intractable. A computationally efficient framework to measure natural frequencies and analyze time histories of 3-D stresses in nonlinear transient structural analyses of rotating fan blades is utilized. This framework uses state of the art tools developed for beam modeling based on VAM and GEBT. The validation of VAM and GEBT against 3-D FEM tool for this current application has been provided in a prior work.[9]

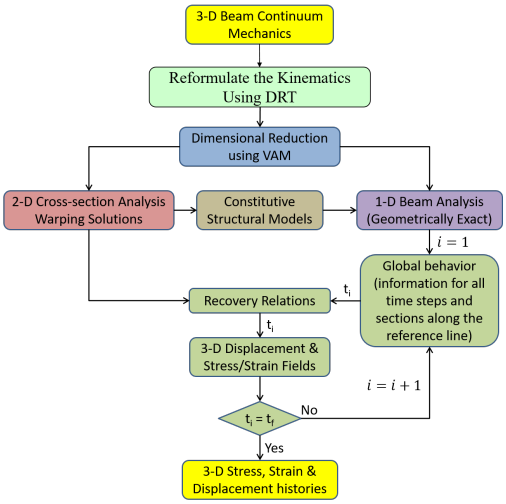

Figure 7. Flowchart representing the structural analysis employing VAM.[13]

Fig. 7 shows the flowchart representing the transient analysis of a structure using VAM. Completely free of ad-hoc assumptions, VAM is used for 2-D cross-sectional analysis which uses the cross section of the geometry in addition to the material properties. VAM when applied to beams splits the analysis into two parts: 1) cross-section analysis, and 2) 1-D beam analysis. Based on VAM, a commercially available tool VABS[14,15] is used to perform the cross-section analysis. 1-D analysis is carried out using GEBT[16] open-source code. On solving, VABS provides the 2-D sectional elastic and inertia constants in the form of 6×6 stiffness and mass matrices, respectively, if a Generalized Timoshenko model-based analysis is invoked. While the sectional stiffness matrix and the mass matrix are the primary output data from a VABS execution, the output files also include solutions to the warping variables which assist in recovery of 3-D variables once the solution of 1-D variables such as the 1-D displacements, forces, and moments are available from GEBT. Further, the information can be used to compute and visualize the stress-strain state on the cross section as well. Given a set of six section stress resultants (the axial force, the two transverse shear forces, the twisting moment, and the two transverse bending moments), which define the load acting on the section's centroid which is represented by the locus of the chosen reference line in the 1-D analysis. Further, with computation of the 3-D recovery variables using VABS, the stress distribution is obtained corresponding to a given time step at a specific cross section. This step can be repeated for all the sections to obtain values for 3-D variables for the entire 3-D geometry. Further details about the procedure and step-by-step explanation is presented by Gupta et al.[17–19]

E. Computation of Structural Constraints

Referring to Fig. 1, the structural analysis block receives the unsteady loads and the blade geometry and checks for structural integrity. The analysis will give a time history of stresses and strains experienced by the blade due to the loads. Stresses, both steady and vibratory, are analyzed. In addition, resonance margins are calculated to ensure that the blade vibrates without the potential of any resonance.

1. *Stress constraint calculation*

In this work, the blade is assumed to be made of an isotropic metal, and hence Von-Mises failure criteria can be applied to check for structural failure. The application of VAM provides a time-history of the six components of stress at each node in every cross-section along the span of the blade. The six components can be combined into the von-Mises stress using

$$\sigma_{VM} = \sqrt{\frac{1}{2}\left[\left(\sigma_{11}-\sigma_{11}\right)^2 + \left(\sigma_{22}-\sigma_{33}\right)^2\left(\sigma_{33}-\sigma_{11}\right)^2 + 6\left(\sigma_{12}^2+\sigma_{23}^2+\sigma_{31}^2\right)\right]} \tag{8}$$

Let us denote the von-Mises stress at time t and at node n_i on cross-section CS_j to be ${}^{CS_j}_{n_i}\sigma^{(t)}_{VM}$. The stresses on the blades will be oscillatory - with a mean stress and some alternating stress. It is necessary to analyze the pair and determine whether it is in the material's operating limit. The steady stress may be well below the tensile stress of the material, but the alternating stresses present may cause the fan to operate outside the envelope allowed for safe operation for a large number of cycles. A simple way of representing this envelope is with the help of a Goodman diagram that draws the envelope of when the material fails. Figure 8 shows a sketch of a Goodman diagram, where the horizontal axis represents the mean stress and the vertical axis represents the alternating stress. Loosely speaking, the line joining the endurance limit (vertical axis) and ultimate tensile stress (horizontal axis) forms the Goodman line. Anywhere inside the region bounded by the Goodman line, the abscissa, and the ordinate, the blade can safely operate for a large number of cycles.

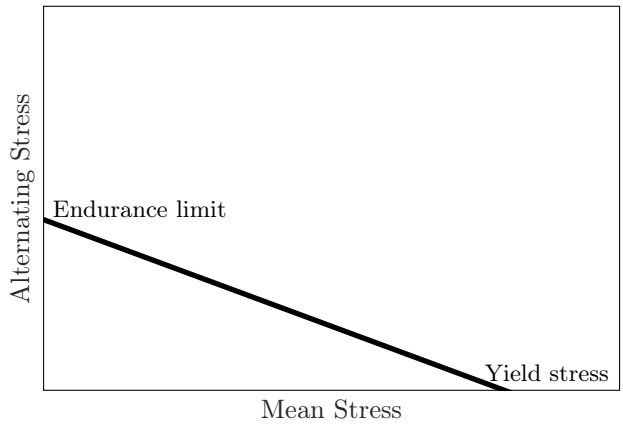

Figure 8. Notional Goodman diagram for blade stresses.

From the time varying stresses contained in ${}^{CS_j}_{n_i}\sigma^{(t)}_{VM}$, mean and alternating stresses can be computed. Each node on the cross-sections of the blade can be plotted on the Goodman diagram. The distance of the line parallel to the limit line (passing through endurance limit and mean stress) and passing through the plotted point can be measured against the distance of the limit line from the origin to compute the margin. One assumption of the work presented here is that the leading edge and trailing edges of the blades are sharp instead of smooth rounded edges. Because of the sharp edges, the maximum stresses might be overestimated. As an effort to prevent producing a much conservative design, a Goodman margin of 80% is set as a requirement for the worst case node of each cross-section.

2. *Resonance margin computation*

There are two frequencies responsible for resonance to occur during forced oscillations - the natural frequency of the blade and the excitation frequency caused by the unsteady loading acting on the blade. The natural frequency of the blade is the frequency at which the blade would vibrate "naturally" when subjected to some disturbance and let to vibrate freely, while the excitation frequency can be determined from the frequency analysis of the blade response when operating in the unsteady loading environment.. There are one or more natural frequencies of all mechanical structures, and resonance can be reached when the excitation frequency reaches any of the structure's natural frequency.[20] Typically, the blades should be designed in such a way that the natural frequency at the design speed should have a safe margin with the frequencies at which the blades are excited at.

Campbell diagram is a simple way of visually analyzing these margins. Figure 9 shows a notional Campbell diagram that can be used to explain its application. The horizontal axis is the speed of rotation and the vertical axis is the frequency. The lines passing through origin are the excitation frequency lines and the curves (almost horizontal lines) are the natural frequencies at different nodes. At the speeds that the blades operate, if any of these two curves cross each other at any point, then resonance is likely to happen if that frequency of excitation occurs. In this present work, a 15% margin is set as a requirement.

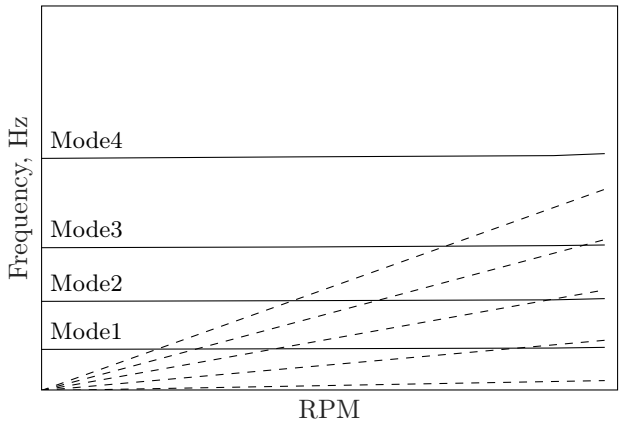

Figure 9. Notional Campbell diagram.

The excitation frequencies are generally engine order multiples. The diagonal lines (possible excitation frequencies), in Fig. 9, are therefore functions of speed of revolution. At any speed of rotation, not all engine order excitations are present. The excitation frequencies can be computed via a Fourier Transform of the displacements. These frequencies are present in the Campbell diagram in the form of engine order excitations and are not dependent on the geometry of the blades, but the amplitudes of these harmonics are. If these frequencies comes in close contact with natural frequency, resonance is expected.

As defined in Section II D, GEBT can be used to obtain the time histories of displacement from unsteady loads. GEBT can also used to run modal analysis and obtain the natural frequencies of the blade. Generally, crossings of concern are in the lower modes of vibration, therefore natural frequencies of first eight modes are evaluated.

F. Design Space: Exploration and Optimization

The successful linkage of all elements discussed above allows for rapid design space exploration of the fan stage. The goal is to identify the tradeoffs between aerodynamic performance and choose a design that maximizes the aerodynamic performance of the fan while respecting the structural constraints. Variables that are chosen for the exploration include the hub to tip ratio of the blade, thickness to chord ratio, radial distribution of thickness to chord ratio, loading type (hub loaded, uniformly loaded, or tip loaded), rotor area ratio, tip chord, chord distribution (or taper), and stator chord. The input variables are designed to change the behavior of flow profiles at the rotor exit, consequently affecting the blade metal angles that define how the stresses act on them. For example, varying hub to tip ratio for a fixed tip diameter affects the incoming Mach number (or velocity), thereby affecting the velocity triangles at the inlet. Changing the loading type redistributed the amount of work imparted by various sections on the blade, thus redistributing the stresses.

Referring to Fig. 1, the information of the constraints and the objective function values enables the optimizer to choose a better set of design variables than the current iteration. At this point, it is relevant to discuss the tools used in the current study. The aerodynamic module is built on the platform of Object Oriented Turbomachinery Analysis Code (OTAC)[21] that outputs the information of blade geometry and loads. The structural analysis tools are wrapped in a MATLAB environment. The computation of constraints involve computing Goodman margin for each cross-section and the resonance margin for each combination of excitation frequency and natural frequency. Presence of discrete variables and large number of gradient requirements make gradient based optimization unattractive. Generating surrogate models for the responses and constraints can be computationally feasible given the low computational time associated with the tools used in this framework.

A design of experiments is created. From the results of the design of experiments, surrogate model of all responses are formed using neural network. Presence of several discrete variables makes polynomial fit more cumbersome. The optimization problem statement is expressed in Eq. 9 . The overall goal is to maximize the design point efficiency of the fan stage. Here, x_s and x_r refers to stator and rotor design variables respectively. Subscript A indicates the variables corresponding to the aerodynamic design only and AS refers to the variables corresponding to both aerodynamic design and structural design. Aerodynamic and structural constraints are enforced. First, it is required that the stage pressure rise is the required pressure rise. At least a small positive value of reaction (≥ 0.05) is desired at the hub. Stall criteria is established by the use of diffusion factor (DF). A DF of 0.6 is considered the threshold value. 80% requirement on Goodman margin (GM) is set for each cross section. A minimum of 5% margin is desired between the excitation frequencies and every mode of vibration.

$$
\begin{aligned}
\min_{\vec{x}_s^A, \vec{x}_r^A, \vec{x}_r^{AS}} \quad & -\eta_{stg} \\
\text{s.t.} \quad & PR_{stg} - PR_{req} && = 0 \\
& -R_{hub} + 0.05 && \leq 0 \\
& DF - 0.6 && \leq 0 \\
& GM_k - 0.8 && \leq 0 \\
& -RM_{i,j} + 0.05 && \leq 0 \\
\text{where} \quad & \\
& i = 1, 2, 3, ...8 && \text{(natural frequency mode)} \\
& j = 1, 2, ...5 && \text{(excitation frequency mode)} \\
& k = 1, 2, 3 && \text{(cross section index)}
\end{aligned}
\tag{9}
$$

III. Test Case Formulation

The test case for this study is a fan blade designed for a distorted flow application using the approach described in Section II A. Note that no structural analysis was performed on this design. The design framework was subjected to a distorted inflow with a total pressure intensity of 0.04. A flow that resembled a sinusoidal profile (distortion intensity = 0.04) was created. Variations in the inlet total pressure along the circumference is shown in Fig. 10, while mass flow and total temperature follow similar variations.

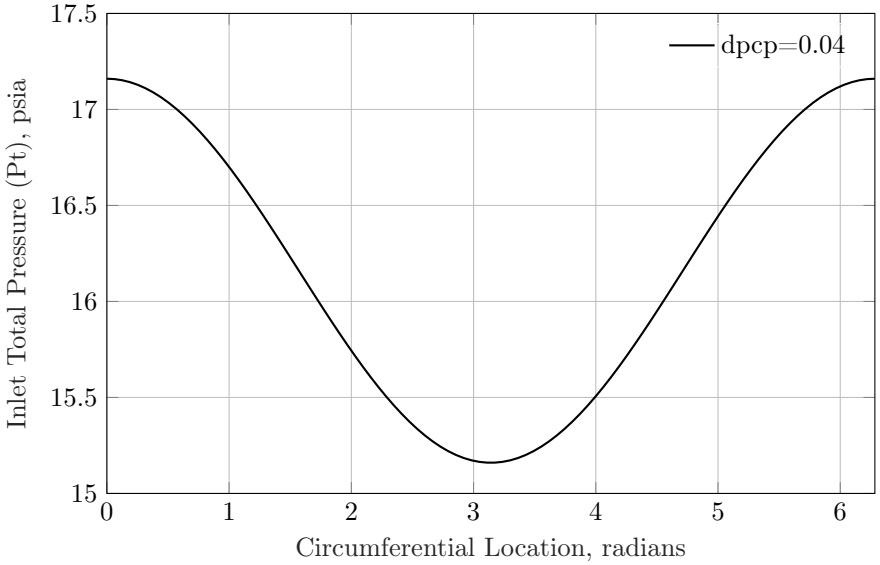

Figure 10. Total pressure profile at the AIP.

Using the framework described in a companion paper,[10] a fan stage with a tip radius of 24 inches and prescribed RPM of 4000 was designed to produce a stage pressure rise of 1.25. A fan stage with a 92.2% efficiency was designed. Assumed material properties for the blade are shown in Table III.

Table 1. Blade material properties.

Material Properties	Value	Unit
Material	Titanium	-
Young's Modulus (E)	116E09	Pa
Poisson's ratio (ν)	0.32	-
Density (ρ)	4506	kg/m^3

Following the process in Section II C, the 3-D representation of the blade was created. Area centroid was chosen as the radial stacking axis. Span-wise and cross-sectional views of the blade are shown in Fig. 11.

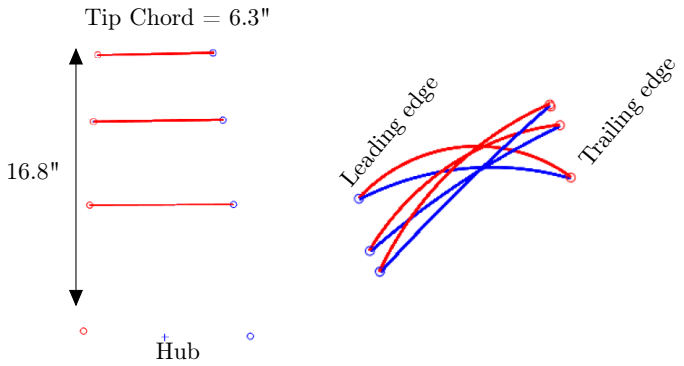

Figure 11. 3-D skeleton of the baseline fan blade.

Following the method described in Section II B, Fig. 12 shows the loads acting on the blade at the hub, mid, and tip for one cycle. It is to be noted that the design loading was higher on the tips; as a result, both tangential and axial loads are more dominant towards the tip. While this blade has been optimized for aerodynamic performance, structural analysis has not been considered. The next section discusses the structural analysis of this design, identifies the optimal design from design space exploration, and shows the results of the structural analysis of the optimized design.

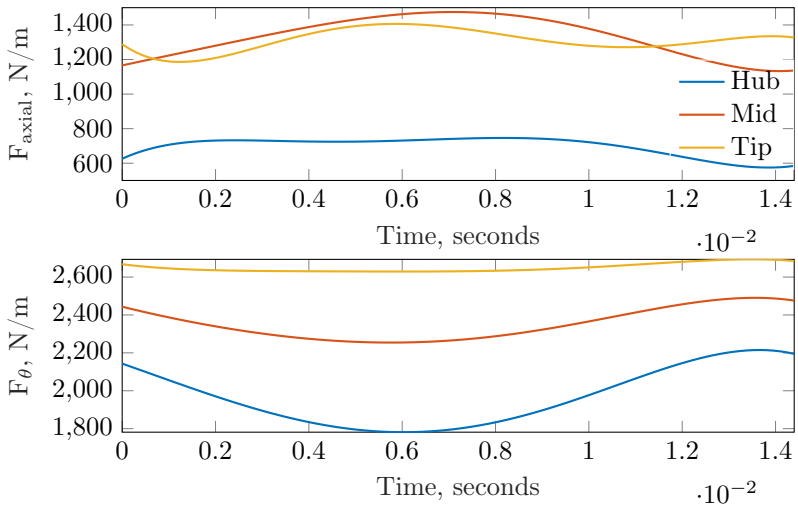

Figure 12. Time varying axial and tangential distribution of loads on the baseline design.

IV. Results

A. Structural analysis of baseline design

With aerodynamic loads and baseline geometry available, the structural analysis of the blade was performed using the method discussed in Section II D. For each node in the cross section, stress components were computed. The mean-alternating stresses pair for the most critical node of each cross-section was plotted on a Goodman diagram and the margin was computed, where the limit line represents 100% margin. Fig. 13 shows the Goodman diagram, where the stresses acting on the three cross-sections are plotted (only the worst node of each cross-section is shown). It can be seen that all cross-sections operate outside the envelope of safe operation by 25%, 11%, and 28% for hub, mid, and tip sections respectively.

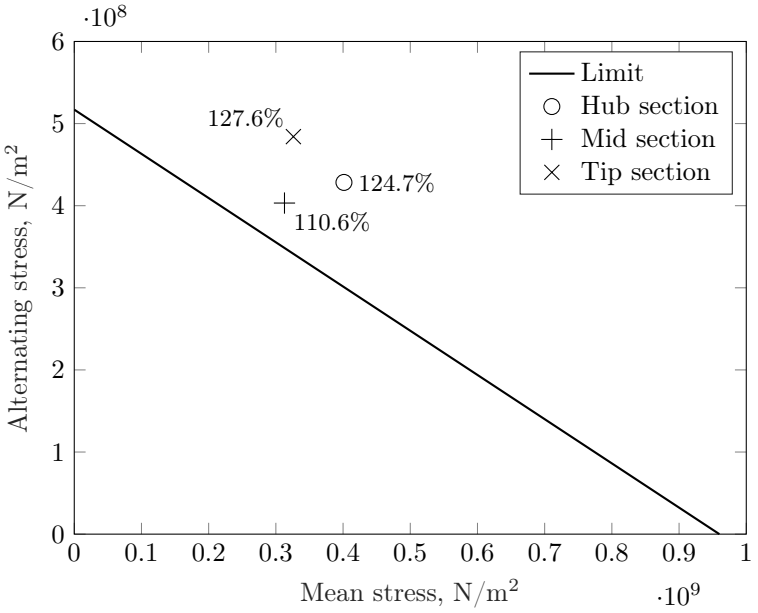

Figure 13. Goodman diagram for the baseline design.

Resonance analysis was performed by first computing the excitation frequencies by the Fourier Transform of the tip displacements in the tangential (u_3) and axial (u_2) directions. As can be seen in Fig. 14, for the u_3 displacement, only the first engine order is the dominant frequency. For the u_2 displacement, the dominant frequencies are 1EO and 5EO. u_1 has virtually no displacement since the root is assumed to be fixed.

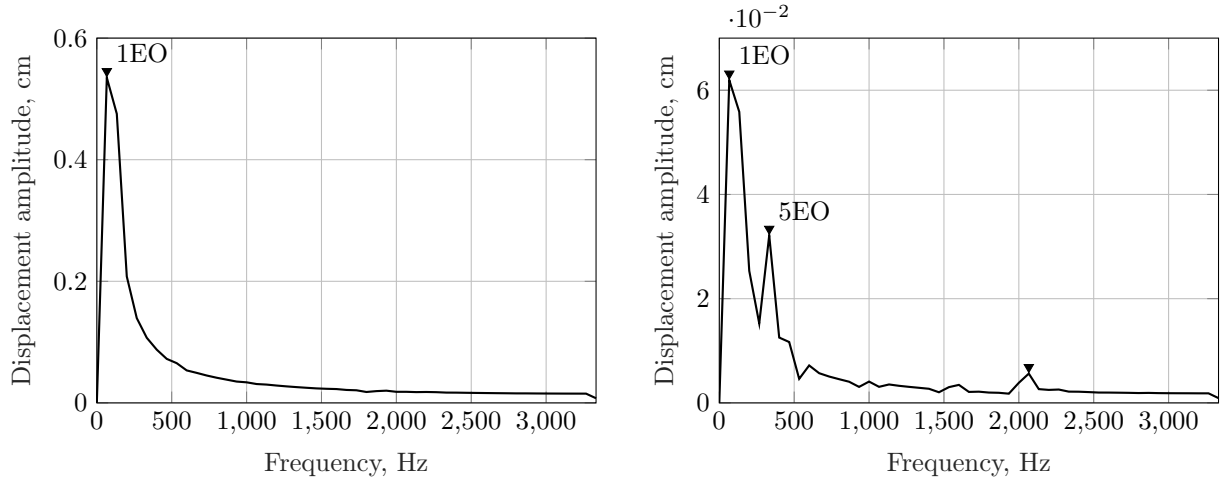

Figure 14. Frequency analysis of tip displacements - u3 [left] and u2 [right].

To evaluate any crossings of concern, natural frequencies for first eight modes were computed by repeating the eigen analysis at various RPMs to establish the mode lines and were plotted on a Campbell diagram as shown in Fig. 15. M2/5EO had a very narrow margin with 0.5% indicating a concern. 28% marigin was present on M1/1EO.

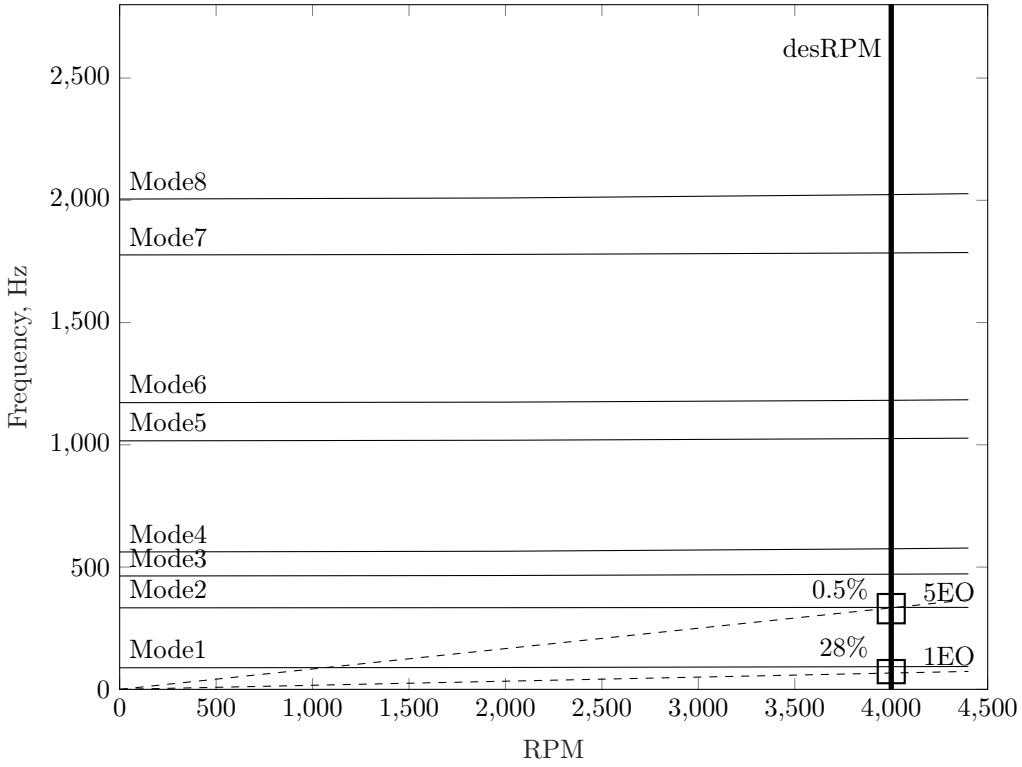

Figure 15. Campbell diagram for the baseline design.

Based on the results of the structural analysis, the rotor blade designed for aerodynamic performance did not meet the structural constraints. Crossings of narrow margin were found through resonance analysis and the blade did not pass the fatigue test as the safety criteria in Goodman diagram was not met for any cross-section.

B. Design space exploration and optimization

In order to explore the design space for the search of an optimal set of design variables, the bounds of design variables were created. Table 2 lists the variables described in Section II F, their corresponding baseline, and lower and upper bounds.

1000 cases using Latin Hypercube Sampling technique were generated, thus 1000 unique designs were created from the aerodynamic block. The geometries and loads information from the outputs of the aerodynamic design module were analyzed in the structural design framework. Natural frequencies were computed for each design. Dynamic analysis resulted in the time varying displacements and stresses, from which the excitation frequencies and mean and alternating stresses were computed.

The presence of multiple categorical variables made neural network a more favorable option for model fitting. The models were created in JMP®, Version <15> SAS Institute Inc. All parameters were fit through one layer network. Three activation functions were used: hyperbolic tangent, linear, and Gaussian. The number of activation functions used and the predictive performance represented by R^2 is shown in Table 3. Aerodynamic stage efficiency and hub reaction metrics showed strong R^2 values and required just a few nodes for fitting. The stall indicator was measured by computing the total number of segments stalled (diffusion factor > 0.6) throughout one cycle time. The number of stalled segments (categorical response) was computed and the probability of any segment stalling was obtained. The Goodman margins for hub, mid, and tip were fit using [3,2,2], [4,2,4], and [4,1,6] hyperbolic tangent, linear and Gaussian functions

Table 2. Bounds of variables for design space exploration.

Categorical Variables		
Parameters	**Baseline**	**Levels**
Design Type	Tip loaded	Hub loaded, uniformly loaded, tip loaded
Taper type	3	1, 2, 3 [no taper to increasing taper]
Thickness distribution along hub to mid span	3	1, 2, 3 [constant to decreasing thickness]
# of blades	23	21, 22, 23, 24, 25

Continuous Variables			
Parameters	**Baseline**	**Lower Bound**	**Upper bound**
Hub to tip ratio	0.3	0.23	0.3
Thickness to chord (hub)	0.104	0.104	0.18
Thickness to chord (tip)	0.08	0.08	0.14
Rotor tip chord	6.39"	6"	8.5"
Rotor exit area ratio	0.95	0.95	0.99
Stator exit area ratio	0.95	0.93	0.97
Stator chord	3.5"	3.5"	5"

respectively. The Goodman margin comprises of two responses: mean stress and alternating stress. It was observed that the predictive performance of the model was lowered due to the difficulty in predicting the vibratory stress component. Efforts to fit resonance margins directly did not result in successful fits. Better fits were obtained when fitting the natural frequencies and excitation frequencies separately and computing the resonance margins afterwards. As can be seen in Table 3, the natural frequencies of all eight modes were strongly predicted by the model with three tanh activation functions. The excitations frequencies were comparatively difficult to fit. It was observed that all excitation frequencies were engine order multiples, so excitation frequencies were modeled as categorical variables with each category defined by a multiple of engine order frequency.

Table 3. Neural network fit of aero-mechanical responses.

Parameter	**Layers**	**Nodes**			R^2 **(training)**	R^2 **(test)**
		HTan	**Linear**	**Gaussian**	**N = 750**	**N = 111**
η_{stage}	1	3	0	0	0.985	0.987
R_{hub}	1	3	1	0	0.949	0.946
P (DF >0.6)	1	3	2	2	0.880	0.840
GM (hub)	1	3	2	2	0.906	0.842
GM (mid)	1	4	2	4	0.860	0.830
GM (tip)	1	4	1	6	0.872	0.863
$f_{nat,i}$ (i=1-8)	1	3	0	0	>0.99	>0.99
$f_{exc,1}$	1	7	5	3	0.935	0.781
$f_{exc,2}$	1	6	0	0	0.887	0.841
$f_{exc,3}$	1	9	0	0	0.913	0.817

The surrogate models developed were used to solve the optimization problem outlined in Eq. 9. A solution that satisfied the optimization criteria was achieved. The optimal set of design variables were then used to evaluate the true aerodynamic performance and true structural constraints. Table B lists the variables and parameters for the optimized design. Note that the blade metal angles and twist are defined in the aerodynamic design module, therefore those variables change consequently.

Table 4. Optimized blade parameters.

Variables	Optimized Value
Design Type	Tip Loaded
Taper Type	1 (no taper)
Thickness distribution (hub to mid)	3
# of blades	25
Thickness to chord (hub)	0.16
Thickness to chord (tip)	0.136
Rotor tip chord	8.5"
Rotor exit area ratio	0.954
Stator exit area ratio	0.957
Stator chord	3.5

The axial and tangential loads acting on the optimized blade are given in Fig. 16. The changes resulting in the optimized design came at a cost of reduction in the stage efficiency by 1.55%. The next section discusses the structural analysis of the optimized design and evaluates if the failure criteria are satisfied.

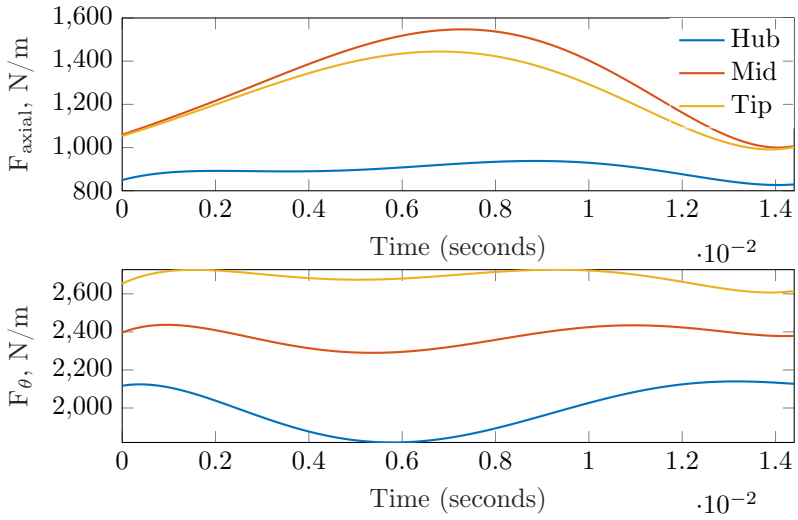

Figure 16. Time varying axial and tangential distribution of loads for optimized design.

C. Structural analysis of the optimized design

Fig. 17 shows the Goodman diagram for the optimized design. All sections of the blade satisfied the 80% Goodman requirement with 78.9%, 78.1%, and 66.5% margins for hub, mid, and tip sections respectively. Several changes were required to achieve this design. Increasing the number of blades helped alleviate some of the stresses, but a trade-off in weight of the system was not considered. Hub to tip ratio was already at the maximum value. Increasing hub to tip ratio helps reduce both vibratory and mean stress, but no room for improvement on that front was available. Thickness and the thickness distribution along the span changed. Tip chord increased from 6.4" from 8.5". It was observed that increasing tip chord reduced the stresses sharply up to 7.4", any remaining increase is likely due to the resonance constraint. The Goodman margins were not highly sensitive to the changes in the exit area ratios.

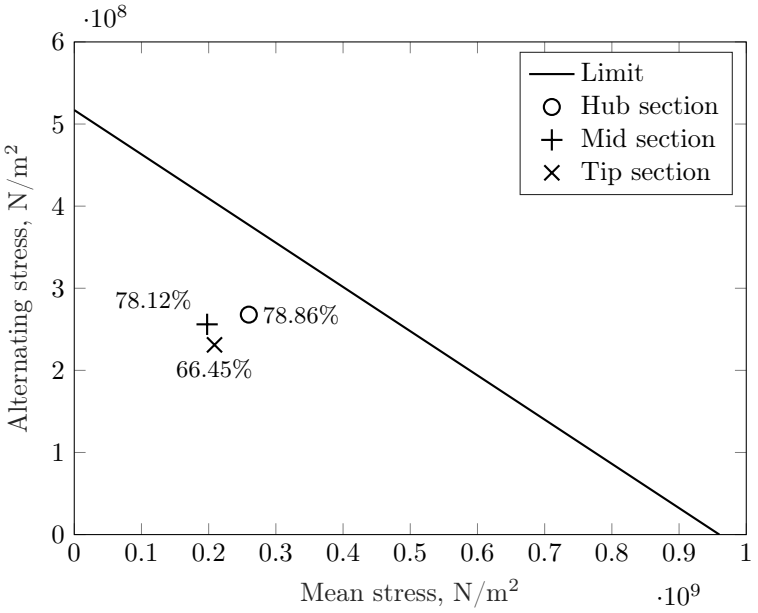

Figure 17. Goodman diagram for the optimized design.

Fig. 18 shows the frequency analysis of tip displacement that was performed to compute the excitation frequencies. The major contributing frequencies were 3EO (200 Hz) for the dominant displacement (u_2) and 3EO (200 Hz), 8EO (533 Hz), and 30EO (2000 Hz) for u_3. Since 2EO excitation was the more dominant one, it is important to ensure there is sufficient margin for that excitation.

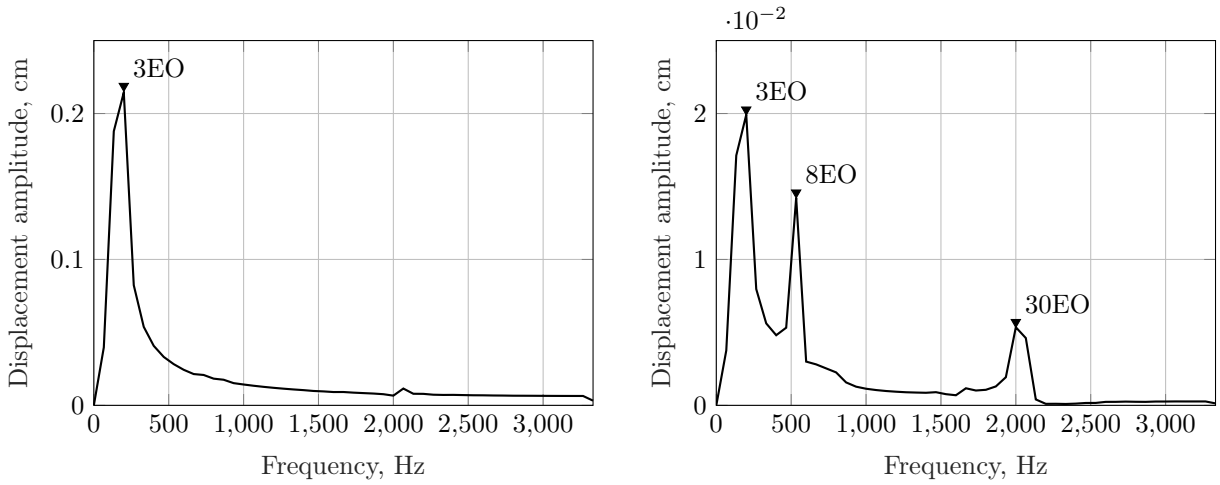

Figure 18. Frequency analysis of tip displacements for optimized design - u3 [left] and u2 [right].

Fig.19 shows the Campbell diagram for the optimized design. Non-excited EO frequencies are omitted for the sake of clarity. It can be seen that 20.6% margin was achieved between Mode 1 and 3EO frequency. M2/8EO and M6/30EO have 5.5% and 8.3% margins respectively. At 4000 RPM, the EO excitation frequencies were only 66 Hz apart. It was very likely that changing the natural frequency would change the excitation frequency to another nearby EO excitation as is apparent from comparing Fig. 14 with Fig. 18. On the baseline design, 1EO and 5EO excitations were present, while in the optimized design, 3EO, 8EO, 30EO were excited. A major concern in the baseline design was that the natural frequencies of modes 2, 3, and 4 were very close to the low EO frequencies, and they were also close to each other. In the optimized design, the natural frequencies increased for all modes. Increasing the thickness and the tip chord caused the natural frequencies to increase. As a result, high order excitations were also observed (30EO). The presence

of taper increased the excitation frequency and reduced the natural frequencies, so the absence of taper helped maintain the difference between the excitation and natural frequencies. Some inherent trade-offs in the satisfaction of Goodman and Cambpell margins were also observed. Increasing taper lowered the Goodman margins, but also lowered the resonance margin. Having the flexibility of the computationally efficient framework allowed to explore these trade-offs and find the true optimal.

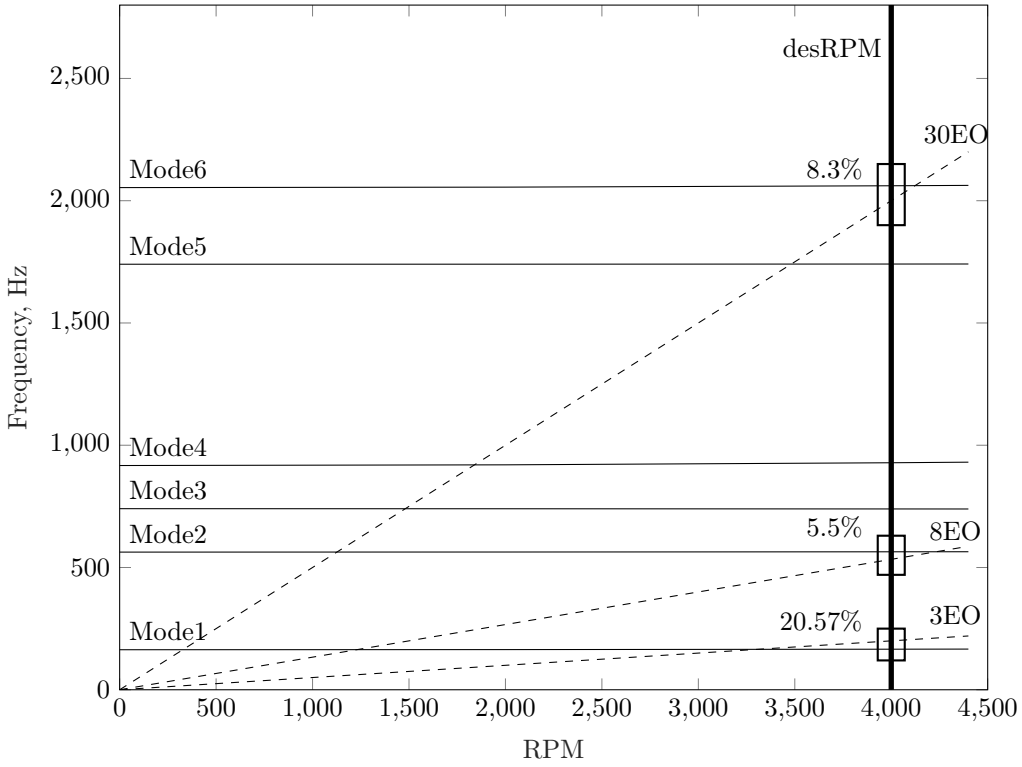

Figure 19. Campbell diagram for the optimized design.

The use of VABS and GEBT in the framework drastically cuts down the time needed to perform time-domain structural analysis. As seen in Fig. 7, VABS is first run to obtain the stiffness and mass matrix for every blade cross-section. The computation of cross-sectional properties are independent of one another and hence can be parallelized. GEBT modal analysis and time-domain displacement analysis are run after VABS. These two operations can also be run in parallel. After obtaining time histories of displacements and loads from GEBT, VABS is run at every time step to obtain the stresses. This is the slowest part of the structural analysis. However, since each time-step in VABS run can be performed independently, making this operation parallel as well. The parallelization described allows for significant reduction in computational time when performing design space exploration. The cases were run on a standard desktop workstation with 4 parallel workers. On average, given a blade geometry and external loads, the entire structural analysis and constraints computation process takes 4 minutes. All 1000 cases were run in about 52 hours.

V. Summary

The conceptual design of fan blades is a multi-disciplinary process considering both aerodynamics and structures. A method to obtain the time-varying external structural loads on the blade was described. To compute the structural constraints, dynamic structural analysis was be performed in a computationally efficient manner. The blade was idealized as a beam and solved using VABS and GEBT. Stress constraints and resonance margins were computed to check the feasibility of the blade. It was seen that a blade designed to have optimal aerodynamic performance did not meet the structural constraints. Trade-offs between the two disciplines necessitated a design space exploration. Optimization was performed and a set of design variables was achieved that maximized the aerodynamic efficiency while satisfying structural constraints.

References

[1]Doulgeris, G., Khaleghi, H., Kalfas, A., and Pilidis, P., "Development of a method for enhanced fan representation in gas turbine modeling," *International Journal of Rotating Machinery*, Vol. 2011, 2011.

[2]Gladin, J. C., *A sizing and vehicle matching methodology for boundary layer ingesting propulsion systems*, Ph.D. thesis, Georgia Institute of Technology, 2015.

[3]Pokhrel, M., Gladin, J., Garcia, E., and Mavris, D. N., "A Methodology for Quantifying Distortion Impacts Using a Modified Parallel Compressor Theory," *ASME Turbo Expo 2018: Turbomachinery Technical Conference and Exposition*, American Society of Mechanical Engineers Digital Collection, 2018.

[4]Marien, T., Welstead, J. R., and Jones, S. M., "Vehicle Level System Impact of Boundary Layer Ingestion for the NASA D8 Concept Aircraft," *2018 AIAA Aerospace Sciences Meeting*, 2018, p. 0271.

[5]Smith, L. H., "Wake ingestion propulsion benefit," *Journal of Propulsion and Power*, Vol. 9, No. 1, 1993, pp. 74–82.

[6]Rodriguez, D. L., "Multidisciplinary optimization method for designing boundary-layer-ingesting inlets," *Journal of Aircraft*, Vol. 46, No. 3, 2009, pp. 883–894.

[7]Cousins, W. T., Voytovych, D., Tillman, G., and Gray, E., "Design of a Distortion-Tolerant Fan for a Boundary-Layer Ingesting Embedded Engine Application," *53rd AIAA/SAE/ASEE Joint Propulsion Conference*, 2017, p. 5042.

[8]Cumpsty, N. and Greitzer, E., "Ideas and methods of turbomachinery aerodynamics: a historical view," *Journal of propulsion and power*, Vol. 20, No. 1, 2004, pp. 15–26.

[9]"Application of Variational Asymptotic Method for Structural Analysis of Fan Rotor Blades in Boundary Layer Ingesting Flow Field, author=Gupta, Mohit and Pokhrel, Manish and Mavris, Dimitri N, booktitle=AIAA SciTech 2020 Forum, year=2020," .

[10]Pokhrel, M., Gladin, J., and Mavris, D., "An Approach for Fan Stage Conceptual Design with Non-axisymmetric Stators in Presence of Distortion [abstract submitted]," *AIAA Aviation*, 2020.

[11]Lambe, A. B. and Martins, J. R. R. A., "Extensions to the design structure matrix for the description of multidisciplinary design, analysis, and optimization processes," *Structural and Multidisciplinary Optimization*, Vol. 46, No. 2, jan 2012, pp. 273–284, 968mw Times Cited:61 Cited References Count:33.

[12]Carta, F. O., "Analysis of Unsteady Aerodynamic Effects on an Axial-Flow Compressor Stage with Distorted Inflow," Tech. rep., Purdue Univ Lafayette in Project Squid Headquarters, 1972.

[13]Hodges, D. H., "Nonlinear Composite Beam Theory," 2006.

[14]Cesnik, C. E. and Hodges, D. H., "VABS: a new concept for composite rotor blade cross-sectional modeling," *Journal of the American helicopter society*, Vol. 42, No. 1, 1997, pp. 27–38.

[15]Yu, W., Hodges, D. H., and Ho, J. C., "Variational asymptotic beam sectional analysis–an updated version," *International Journal of Engineering Science*, Vol. 59, 2012, pp. 40–64.

[16]Hodges, D. H., "Geometrically exact, intrinsic theory for dynamics of curved and twisted anisotropic beams," *AIAA journal*, Vol. 41, No. 6, 2003, pp. 1131–1137.

[17]Gupta, M., Sarkar, K., and Hodges, D. H., "3-D Stress-Strain Histories for Composite Beams in Nonlinear Transient Structural Analysis," *AIAA Scitech 2019 Forum*, 2019, p. 1026.

[18]Gupta, M., Sarojini, D., Shah, A., and Hodges, D. H., "Beam Theory for Asymptotic Analysis of Aperiodic and Inhomogeneous Structures," *AIAA Journal*, 2019, pp. 1–14.

[19]Sarojini, D., Gupta, M., Hodges, D. H., and Mavris, D. N., "An Efficient Method to Dimensionally Reduce Aperiodic Inhomogeneous 3-D Structures to 1-D Beam-Like Structures," *AIAA Scitech 2020 Forum*, 2020, p. 0272.

[20]Halliday, D., Resnick, R., and Walker, J., *Fundamentals of physics extended*, John Wiley & Sons, 2010.

[21]Jones, S. M., "Development of an object-oriented turbomachinery analysis code within the npss framework," 2014.